Metal–silicate partitioning of U: Implications for the heat budget of the core and evidence for reduced U in the mantle

Authors: Bethany A. Chidester[a,*], Zia Rahman[b,c], Kevin Righter[c] and Andrew J. Campbell[a]

Affiliations:
[a]Department of the Geophysical Sciences, University of Chicago, Chicago, IL 60637

[b]Jacobs, NASA Johnson Space Center, Houston, TX 77058

[c] NASA Johnson Space Center, Houston, TX 77058

*Correspondence to: chidesterba@uchicago.edu

Submitted to Geochimica et Cosmochimica Acta, August 5, 2016; Revised November 1, 2016; Accepted November 20, 2016

Abstract

Earth's core might require an internal heat source, such as radioactive decay, to explain the presence of the magnetic field through geologic time. To investigate whether U would be an important heat source in the core, we performed metal–silicate partitioning experiments of U at *P-T* (up to 67 GPa and 5400 K) conditions more relevant to a magma ocean scenario than has previously been reported. This study finds the partitioning of U to be strongly dependent on fO_2, temperature, the S content of the metal and the SiO_2 content of the silicate during core-mantle differentiation. Differentiation at mean conditions of 42-58 GPa and 3900-4200 K would put 1.4-3.5 ppb U (2-8 wt% S) in the core, amounting to a maximum of 1.4 (+1/-0.7) TW of heat 4.5 billion years ago. This is likely not enough heat to mitigate early widespread mantle melting. It was also found that U likely exists in the 2+ oxidation state in silicate melts in the deep Earth, a state which has not been previously observed in nature.

1. Introduction

The Earth is a heat engine, driven by secular cooling, radioactive decay and the segregation and solidification of materials into distinct layers (Verhoogen, 1980). Of these heat sources, the decay of the long-lived radioactive isotopes ^{235,238}U, ^{232}Th and ^{40}K account for up to half of the total heat flux at the surface of the planet (Lay et al., 2008). The distribution of these elements in the deep Earth may have profound implications for the heat budget of the core, including the age of the inner core and the source of the geodynamo that has driven the Earth's magnetic field through geologic time, as well as the thermal evolution of the mantle (Labrosse et al., 2001). Whether these radioactive elements are an important heat source in the core itself has been uncertain. Based on the strongly lithophilic nature of these elements at ambient conditions, it has been considered unlikely that they would partition into the metallic phase as the core segregated (McDonough and Sun, 1995). However, it is difficult to reconcile the presence of a geomagnetic field prior to the initiation of the inner core without this heat source, because the temperatures required for a purely thermally driven dynamo early in Earth's history are unreasonably high (Nimmo, 2015). This problem has become even more pressing as recent calculations (de Koker et al., 2012; Pozzo et al., 2012; Pozzo et al., 2014) and experiments (Gomi et al., 2013; Seagle et al., 2013; Ohta et al., 2016) have shown that the thermal conductivity of iron and iron alloys at outer core conditions could be 2-3 times higher than formerly believed, although uncertainty persists on this issue (Konôpková et al., 2016). If a radiogenic heat source were present, the core would cool more slowly, the inner core would be somewhat older, and the inferred initial temperature of the core would be more reasonable. It has been suggested that the extremely high temperature conditions of core formation could cause even highly lithophile elements

such as Mg to partition into the metallic core (Badro et al., 2016; O'Rourke and Stevenson, 2016). This leads one to reconsider whether other lithophile elements such as U, Th, K, and rare-earth elements (REE) might also partition into the core in significant amounts, and thus, explain isotopic deviations of REE in surface rocks with respect to the chondritic building blocks of the planet (e.g. Boyet and Carlson, 2005).

Previous high pressure, high temperature metal–silicate partitioning experiments have shown that U will partition into the metallic phase at very low oxygen fugacity (fO_2) and high S content, but that under the P-T-fO_2 conditions of Earth's upper mantle, the partitioning is too low for U to be an important heat source in the core (Malavergne et al., 2007; Bouhifd et al., 2013). However, these experiments were done at relatively low pressures and temperatures (i.e. $P \leq 20$ GPa and $T \leq 2700$ K). To match the mantle abundances of the siderophile elements such as Ni and Co, equilibration of the metal in a magma ocean would have had to take place at much deeper conditions on average (i.e. P between 30 and 60 GPa, with T up to 4200 K) (Li and Agee, 2001; Bouhifd and Jephcoat, 2011; Siebert et al., 2012; Fischer et al., 2015; Righter et al., 2016). Wohlers and Wood (2015) recently suggested that a significant amount of U (and other nominally lithophile elements) could have partitioned into sulfides at very reducing conditions in the solar nebula, and that by incorporating those sulfides into the growing core early in planetary accretion, those elements would have been trapped in the core even as the whole planet was continuously becoming more oxidized and S-depleted. That model relies on a very specific scenario for planetary growth, and it is necessary to consider more broadly the conditions under which heat-producing elements could have entered the core as the planet was growing. Thus, it is important to investigate the partitioning of U at higher pressures

and temperatures such that the partitioning behavior of U can be investigated within the *P-T* space of a deep magma ocean. Here, we demonstrate that under magma ocean conditions, U becomes less lithophile, and could have altered the energy budget of the core if equilibration in a magma ocean occurred at very high temperatures.

2. Experimental Methods

2.1. Sample preparation and laser heating

Metal–silicate partitioning experiments were conducted in the laser-heated diamond anvil cell (LH-DAC) at the University of Chicago. The silicate used in most experiments was a mixed oxide powder having a major element composition of pyrolite (with or without Ca) (McDonough and Sun, 1995), but without any FeO to keep conditions as reducing as possible, and with elevated levels of UO_2 to facilitate analysis of the experimental products (Table 1). In two cases (B22 and B23) the silicate was composed of a mixture of UO_2, ThO_2 and SiO_2. MgO (99%), Al_2O_3 (99.99%), SiO_2 (99.9%), $CaSiO_3$ (meta, reagent grade), Fe (99.9+%, <10 μm), FeSi (99.9%) and FeS (99.9%) were all purchased from Alfa Aesar. To remove any contaminating OH from the oxide and silicate powders, they were fired in a furnace at 1000 ˚C for 12-20 hours prior to use. ThO_2 (99.99%) was purchased from Strem Chemical. Depleted UO_2 powder was purchased from SPI Chemical. This material contained a small amount of polymer binder, so it was washed in ethanol and baked at 100 ˚C prior to sample preparation. The silicate and oxide materials were mixed together in the proportions shown in Table 1, and ball-milled in a tungsten carbide (WC) capsule at 20 Hz for 1.5 hours. The metal used in these experiments was either stoichiometric FeSi or a mixture of FeSi, FeS and Fe, to produce Fe alloys of targeted compositions during the experiment. The metals were also

99 blended in a WC capsule using a ball mill at 20 Hz for 1.5 hours. Tungsten was not
100 detected in any of the samples; however, it is possible that trace W was introduced during
101 the ball milling processes and that it was not observed as a result of a strong peak overlap
102 between W and Si using energy dispersive analytical techniques.
103 Oxygen fugacity is not controlled externally in laser heated diamond anvil cell
104 experiments; this is precluded by the nature of the experiments (~10 μm x 30 μm
105 diameter laser heated spot, confined between diamond anvils). Similarly, due to the very
106 small scale of the samples, one cannot precisely control a priori the exact proportions of
107 metal and silicate in each sample. Here, as in previous metal–silicate partitioning
108 experiments at very high *P-T* conditions, the oxygen fugacity of the system is self-
109 buffered by exchange of Fe and Si between metal and silicate melts. We influenced this
110 self-buffering toward reducing conditions by using starting materials with high Si
111 contents in the metal, but as recognized previously (Siebert et al., 2012; Fischer et al.,
112 2015), the Fe-Si exchange reaction at high *P-T* conditions drives the oxygen fugacity of
113 the experimental products toward a relatively narrow range of ΔIW conditions.
114 Importantly, we measure the composition of coexisting metal and silicate products to
115 establish the fO_2 that was achieved in the experiments.
116 Diamond anvil cell samples were loaded into stainless steel gaskets pre-indented
117 to 18-23 GPa or rhenium gaskets pre-indented to 25-28 GPa. The diamond culets
118 measured 300 or 250 μm in diameter. The metallic sample material was pressed into a
119 thin foil of ~2-5 μm thick, and encapsulated with flakes of silicate powder. Samples B22
120 and B23 were prepared as extreme end-members using a mixture of UO_2, ThO_2 and FeSi
121 as the pressed flake and SiO_2 was used as the surrounding silicate. A small amount of

122 Al_2O_3 was introduced in these two samples by processing in a corundum mortar and
123 pestle. The samples were dried at 90 ˚C for 30-60 minutes after loading but prior to
124 closing the cell, to remove any adhered moisture from the sample. The pressure at the
125 location to be heated was determined using the Raman shift of diamond (calibrated to
126 ruby under quasi-hydrostatic conditions after Akahama and Kawamura, 2007) prior to
127 heating. Several pressure measurements were made across each sample chamber, and
128 they were found to be within 1-2 GPa on average, indicating reasonably constant stress
129 state across the small sample chamber. Any non-hydrostatic strain is expected to be
130 eliminated at the high temperatures of melting. Thermal pressure was estimated from two
131 additional samples of the same geometry under the same pressure range that were laser
132 heated with in situ synchrotron X-ray diffraction to be ~20% of the room temperature
133 pressure (Fischer et al., 2015). The pressures listed in Tables 2 and A.1 include the 20%
134 thermal pressure for all samples in this study. The error on pressure was determined
135 based on uncertainties in the thermal pressure and in the diamond Raman measurement.
136 The laser heating system used for these experiments is a double-sided version of
137 that described by Campbell, 2008. Samples were compressed to the target pressure, then
138 laser-heated on both sides using a 1064 nm Yb-doped fiber laser. Temperature was
139 gradually increased to above the sample liquidus over a period of ~5 minutes. Samples
140 were held at the maximum temperature for 15-30 seconds, then quenched to room
141 temperature to conserve the high-temperature chemical distribution by turning off the
142 laser. Average temperature in these experiments was measured spectro-radiometrically
143 with 5-10 msec spectral exposures, while temperature gradients were simultaneously

144 assessed using a four-color spectral imaging system with a 200-500 msec exposure time
145 (Campbell, 2008).

146 ***2.2. Sample recovery***

147 The samples were decompressed over ~30 minutes and then secured within the
148 gasket to a 0.5" aluminum SEM pin stub. They were then coated with a thin (~10 nm)
149 layer of carbon to provide a conductive surface for imaging with an electron beam. The
150 samples were sectioned along the axis of compression through the center of the laser-
151 heated spot using a dual beam focused ion beam (FIB) at Johnson Space Center (FEI
152 Quanta 3D FEG). The FIB sections of each sample were attached to a copper TEM grid
153 and typically thinned to ~1 μm.

154 ***2.3. Chemical analysis***

155 Chemical analysis of the samples was done at the University of Chicago using
156 energy dispersive X-ray spectroscopy (EDX) on either a JEOL 5800LV or Tescan Lyra3
157 scanning electron microscope (SEM) at 15 keV and ~2 nA. Using the JEOL instrument,
158 several profiles were taken across each sample with measurements every 0.25 μm and 2
159 minutes/step. Using the Tescan instrument, profiles were taken in 20 nm steps with a 10
160 ms dwell time per pixel and a total of 350 passes over the profile. Compositions were
161 determined by averaging all of the point measurements from each respective phase. The
162 measurements reported in this study are very precise due to a large number of
163 measurements made in each phase. Based on measurements of analytical standards, the
164 sample measurements are expected to be accurate to within 5% (relative), but this
165 calibration inaccuracy is expected to be similar for both the metal and the silicate phase,
166 so will cancel out in the partition coefficient calculations. Detection limits for Al, Ca, Mg

and U in the metallic phase were determined as 3 times the background. These measurements were made in the metallic phase of sample B59, which contained all of these elements in concentrations too low to be detected by EDX. Detection limits are dependent on the number of measurements made in each phase because of counting statistics. For the metals in the samples reported here (13-261 measurements) the range of detection limits is: 0.04-0.18 atom% Al, 0.03-0.15 atom% Ca, 0.06-0.28 atom% Mg and 0.02-0.09 atom% U. X-ray maps of select elements were obtained for sample B42 (Fig. 1) using the JEOL 2500SE field emission scanning transmission electron microscope (STEM) at Johnson Space Center.

In several cases, the silicate melt region was small compared to the activation volume of the EDX measurements. In these cases, we were able to deconvolute the signals from each phase using a point-spread function. Each point measurement was treated as an integration over an area having a Gaussian-weighted signal, and the composition of the silicate melt was fitted to a line profile across each phase (Fig. A.1). Other fitted parameters in this analysis included the location of the boundary between the silicate and metallic melt phases, the width of the Gaussian (σ), and if necessary, the composition of the silicate mineral in the outer region of the laser heated spot. The Mathematica code and example data are provided (ExamplePSA.nb and ExamplePSA_data.csv in the Supplemental Information). For those samples whose compositions were fit in this way, the uncertainties provided are the standard errors to the fit.

Because the samples were thinner than the activation volume of the EDX measurement, the analyses were normalized to 100%. Oxide mole fractions in the silicate

190 melt were calculated stoichiometrically using the following oxidation states: 6+ for S; 4+
191 for Si and Th; 3+ for Al; and 2+ for Fe, Mg, Ca and U (See Section 4.1). Oxygen
192 measurements in Fe-rich alloys are often challenging using EDX because of a slight
193 overlap in excitation energy between the O $K\alpha$ line (0.525 keV) and the Fe $L\alpha$ line
194 (0.705 keV), but it is known that a significant amount of O will partition into Fe metals at
195 high *P-T* conditions (Frost et al., 2010; Fischer et al., 2015), so it is necessary to obtain
196 accurate O contents in the metals in these experiments. The Tescan system at the
197 University of Chicago is equipped with a silicon-drift detector (Oxford Instruments X-
198 Max^N) that has sufficient energy resolution to fully deconvolute these Fe and O peaks.
199 Measurements on several Fe-bearing silicate and oxide standards on this instrument
200 showed the O measurements to be accurate to within 5% (relative). Furthermore, there
201 was no significant difference in the silicate melt compositions of our samples when they
202 were calculated as stoichiometric oxides or when measuring O as a separate element.
203 Finally, the oxygen content in the metal phase of each sample was compared to the
204 expected O content from the published *P-T* dependence of O partitioning between
205 peridotite and metal (Fischer et al., 2015), and most were found to be within 15% of
206 those predicted values. Samples B42, B50 and B56 were not measured using the silicon-
207 drift detector, so the reported metal compositions for these samples were obtained by
208 measuring all elements except O in the EDX, and renormalizing with the O content
209 predicted by the O partitioning parameters at the relevant *P-T* conditions (Fischer et al.,
210 2015).

211 **3. Results**

212 ***3.1. Sample texture***

213 Metal–silicate partitioning samples were sectioned to ~1 μm thick for observation
214 in the SEM. Figures 1 and 2 show representative samples after sectioning. The samples
215 always consisted of a quenched round metal melt ball surrounded by a quenched silicate
216 melt. There was a region of silicate material, often of bridgmanite composition, outside
217 the silicate melt that was clearly recrystallized during heating. The laser-heated spots
218 were on the order of 20 μm in diameter. There was no evidence of immiscible metallic
219 phases, in contrast to the Fe-S-Si miscibility gap observed below 15 GPa (Sanloup and
220 Fei, 2004). The metal phase often exhibited a uniform quench texture, where Si and O
221 that were soluble in the metal at high temperature exsolved upon rapid cooling. Due to
222 the rapid quench rates in the diamond anvil cell, no strong quench texture was observed
223 in the silicate melt. That the boundaries between each phase (metallic melt, silicate melt
224 and silicate mineral) were always smooth and continuous is evidence that the system
225 within the laser-heated spot had a minimal free energy, i.e. was locally equilibrated under
226 the high *P-T* experimental conditions. Further demonstration of local equilibrium was
227 that the composition of the silicate was uniform over sample regions of different scales,
228 indicating that kinetic processes like thermal diffusion were not a problem.

229 ***3.2. Chemical composition and oxygen fugacity***

230 The pressure, temperature and relative fO_2 conditions of each sample from this
231 study are listed in Table 2, and together with all literature data used in this study in Table
232 A.1. The compositions of each phase of each sample in this study and their errors are
233 reported in Tables 3 (metal phase) and 4 (silicate phase) and are provided as text files
234 (Tables A.2 and A.3) in the Supplemental Material for ease of use. Here, fO_2 was
235 calculated in reference to the iron-wüstite buffer assuming ideality (i.e. that the activities

of Fe in the metal and FeO in the silicate were equal to their mole fractions in their respective phases), such as:

$$\Delta IW = 2Log_{10}\left(\frac{X_{FeO,silicate}}{X_{Fe,metal}}\right) \quad \text{equation (1)}$$

To evaluate the effect of the high concentrations of Si and O in the metal phases of our samples, we also calculated this parameter using the activity of Fe (a_{Fe}) from the online metal activity calculator (http://www.earth.ox.ac.uk/~expet/metalact/; based on Wade and Wood, 2005) in place of $X_{Fe,metal}$. This calculator failed to compute a result for several of our samples at very high temperatures. However, thermodynamic results using the model activities that were possible to compute were virtually unchanged using this model, except that the residuals to the fit appeared to trend slightly with temperature. Thus, we conclude that this type of model is not yet calibrated to sufficiently high temperatures for this study, and for now unnecessary given other uncertainties in our experiments. For consistency, the literature values for fO_2, as well as partition and exchange coefficients, were recalculated using mole fractions of elements and oxides converted from the weight percents reported.

As mentioned previously, compositions of each phase were obtained from point measurements in profile across the laser-heated spot. An example of this type of measurement is given in Fig. 2. In all cases, U was measurable in the silicate melt and within the metallic region, but was usually not measurable in the crystalline bridgmanite outside of the melt region. This demonstrates very low compatibility of U in crystalline bridgmanite (Corgne et al., 2005), as well as the significant partitioning of U into Fe metal at these high pressures and temperatures. It is notable that Th was present at relatively high levels in two of the experiments listed here, B22 and B23, but was not

measurable in the metallic phase of either sample. This indicates a dichotomy between the chemical behaviors of Th and U, which are otherwise quite similar.

It can be seen in Fig. 2b that in sample B50, recovered from 56 GPa and 4700 K, both U and Ca concentrate in the silicate melt, and that U partitions into the metal but Ca does not. A concern raised for measurement of metal–silicate partitioning samples from the laser-heated diamond anvil cell is that the spatial scale is too small, and the measurement is contaminated with fluorescence from a higher abundance region (Wade and Wood, 2012). In this regard, comparison of U chemical profiles with those of Ca is particularly important. Ca and U have similar absorption energies in EDX (3.164 and 3.690 kV for the U $M\alpha$ line and the Ca $K\alpha$ line, respectively); thus, if the measurements in the metal were artificially high due to fluorescence from the silicate, we would expect to see it with both elements, but this is not observed. Indeed, the apparent abundance of U in the silicate mineral directly outside the silicate melt is lower than that measured in the metal. We conclude that secondary fluorescence has not compromised our measurements of U in the metal phase in these experiments.

4. Discussion

4.1 Thermodynamic Modeling and the oxidation state of U

Partition coefficients for U between metal and silicate were calculated as

$$D_U = \frac{X_{U,metal}}{X_{UO_{n/2},silicate}} \quad \text{equation (2)}$$

where X_i are the mole fractions of those species in their respective phases and n is the oxidation state of the U cation in the silicate melt. The partition coefficient is not only dependent on thermodynamic variables such as temperature and pressure, but also on composition and the fO_2 of the system. Because of this, a multivariate approach is

necessary to address all of the variables simultaneously. The dependence on redox condition is best described by considering the exchange reaction

$$UO_{n/2} + \frac{n}{2} Fe \leftrightarrow \frac{n}{2} FeO + U \quad \text{equation (3)}$$

in which uranium (having valence *n*) is reduced to a metal by exchanging oxygen with iron, the most abundant multivalent element in Earth's interior. The exchange coefficient for this reaction,

$$K_D = \frac{X_U / X_{UO_{n/2}}}{\left(X_{Fe} / X_{FeO}\right)^{n/2}} = \frac{D_U}{\left(D_{Fe}\right)^{n/2}}, \text{ equation (4)}$$

is thus a useful means of describing the dependence of U partitioning on *P*, *T*, and composition of the various phases independent of the redox state. However, use of the exchange coefficient requires that the oxidation state of U be assumed or inferred from the fit to the data. Previous studies (Malavergne et al., 2007; Bouhifd et al., 2013) have inferred a U oxidation state of 4+, which is reasonable given that the most reduced form of U at surface conditions is 4+. However, this assumption did not work well for fitting the combined high-pressure and low-pressure data here.

When fitting the dependence of partition coefficient (D_U) on fO_2 explicitly, as in Eq. 5,

$$Log_{10} D_U = a + \frac{b}{T} + c\frac{(1 - X_S)^2}{T} + d\frac{(1 - X_{SiO_2})^2}{T} + e\Delta IW \quad \text{equation (5)},$$

we find that the U oxidation state within the silicate liquid at these conditions is best described as 2+, instead of the 4+ valence that has previously been inferred. Here, X_i is the mole fraction of species *i*, and *a* and *b* are representative of the entropy and enthalpy

302 of the reaction in Eq. 3, respectively. The compositional terms are expressed as the
303 excess Gibbs free energy of mixing in a Guggenheim-type binary mixing model (e.g.
304 Ganguly, 2009), where the log of the activity coefficient (γ_i) equals a constant times (1-
305 $X_i)^2/T$. Equations 5 and 6 neglect any and all terms that were found to be statistically
306 insignificant to the partitioning of U, including pressure and other compositional effects,
307 discussed later. In this notation, the coefficient e is equal to negative one quarter of the U
308 oxidation state in the silicate liquid. The parameters for this fit are listed in Table 5,
309 where $e = -n/4 = -0.49$. Thus, the inferred oxidation state, n, for U in the silicate melt is
310 indeed 2+. To show this result more explicitly, we corrected all of the data using the
311 fitted parameters in Eq. 5 to single temperature (3000 K), S content in the metal (2 wt%)
312 and SiO_2 content in the silicate (0.45 wt%). These data were then plotted in Fig. 3 as
313 corrected $Log_{10}D_U$ versus the measured ΔIW values. The slope of this line is indeed -
314 0.49, consistent with U^{2+}. A line with slope of -1 (indicating a 4+ oxidation state for U) is
315 also shown for reference. The data used in this regression are listed in Table A.1.
316 This surprising result has only been previously observed using relatively exotic
317 organometallic synthesis methods (MacDonald et al., 2013) and is consistent with recent
318 papers that have reported a reduction in oxidation state of two other high-field strength
319 elements, Nb and Ta, in silicate melts at 5 GPa under reducing conditions (Cartier et al.,
320 2014; Cartier et al., 2015). These results indicate that metal–silicate partitioning of these
321 elements is less dependent on fO_2 at high P-T conditions. This change in U valence could
322 explain the difference in partitioning behavior between U and Th in the two experiments
323 that contain both elements. This is also likely important for mineral–melt partitioning of
324 these elements at depth within the Earth, as cations with lower field strength are more

likely to be compatible in mantle minerals (Blundy and Wood, 2003). We propose that this could be a mechanism for fractionation between U and Th at high *P-T* conditions and should be investigated further.

4.2. Comparison with previous data

A comparison of our high-pressure exchange coefficients to earlier work (Malavergne et al., 2007; Bouhifd et al., 2013) in Fig. 4 shows a strong dependence of K_D on temperature. This dependence was not discernable in earlier studies, likely because of the relatively small pressure and temperature ranges previously investigated. Much of the scatter in Fig. 4 relates to other factors, besides temperature, that affect the metal–silicate partitioning of U. To parse the dependence of partitioning on pressure, temperature and chemical composition of the metal and the silicate, the K_D data were fit to an equation of the form

$$Log_{10}K_D = a + \frac{b}{T} + c\frac{(1-X_S)^2}{T} + d\frac{(1-X_{SiO2})^2}{T} \quad \text{equation (6)}$$

where the coefficients are thermodynamically equivalent to those in Eq. 5, except that the fO_2 term is accounted for in K_D. These coefficients are listed in Table 5, and are found to be identical to those in Eq. 5.

Our results show that, within the range of conditions appropriate to core formation in Earth, temperature is the factor that most strongly influences metal–silicate partitioning of uranium. Sulfur in the core appears to be favorable for U partitioning into the metal, while SiO_2 in the silicate has a strong negative effect. In this context, SiO_2 content of the silicate melt is a proxy for how polymerized the melt is, which is often a consideration in partitioning studies at lower pressures and temperatures (O'Neill and

347 Eggins, 2002; Righter, 2003). The effect of pressure was found to be insignificant, and is
348 not included in the reported parameterization.
349 The concentrations of UO_2 in the silicate melts of these samples are far greater
350 than the very low (ppb to ppm) levels that occur in natural silicates. This was necessary,
351 as the available techniques for measuring composition at such high spatial resolution do
352 not have the capability of detecting elements at such low concentrations. Consequently, it
353 is important to consider that these samples may not fall within the Henry's Law range of
354 chemical activity; i.e. the activity of U, and therefore its partitioning behavior, is different
355 (either higher or lower) than it would be in nature. This would be accounted for in the
356 thermodynamic model in the same way that we have accounted for S and SiO_2, with a
357 coefficient on the composition term to describe the non-ideality of the solution. Despite
358 the range of UO_2 (or U) concentrations in the silicate (or metal), it was found that such a
359 term was not statistically significant. Thus, we concluded that the high concentrations of
360 UO_2 in our samples do not affect the observed partitioning of U. Likewise, it was found
361 that additional terms in equations 5 and 6 to account for the Si content for the metal were
362 also not significant. Thus, the activity coefficients of UO_2 and Si appear not to vary
363 strongly over the range of compositions explored in this study, and we tentatively
364 conclude that Henry's Law violations do not impact our results. Further examination of
365 this issue would benefit from trace elemental analyses, probably on multianvil press or
366 piston-cylinder experiments.
367 In all the experiments described here, as well as many of those reported in the
368 literature, the metallic phase has the opportunity to be completely saturated in carbon due
369 to reaction with the sample containment (either graphite capsules in multi-anvil or piston

cylinder press, or diamonds in the diamond anvil cells). Unfortunately, in addition to being a ubiquitous environmental contaminant, C is difficult to measure using the spectroscopic techniques described here. However, there is very little evidence that C is actually an important factor for metal–silicate partitioning of U. The interaction parameter between C and U in a C-saturated iron alloy is listed in the Steelmaking Data Sourcebook as 0 at temperatures around 1600-1700 K (Japan Society for the Promotion of Science and the 19th Committee on Steelmaking, 1988). Furthermore, Bouhifd et al. (2013) completed metal–silicate partitioning experiments of U at moderate pressures in both MgO and graphite capsules and found C to have a negligible effect. They, along with others (Miettinen, 1998; Kawanishi et al., 2009; Li et al., 2015), show that the C and Si contents of the metallic phase are inversely correlated. Thus, given the high Si contents of the metals in our study, and the negligible interaction between U and C, we expect our parameterization to be accurate without including a parameter for the effect of C content.

4.2 Core formation at a single effective pressure and temperature

We use this parameterization of U partitioning with a differentiation model to place bounds on the U content of the Earth's core. Using average *P*-*T* conditions of core-mantle equilibration (Siebert et al., 2012; Fischer et al., 2015), that is P = 45-58 GPa and T = 3900-4200 K (the liquidus of peridotite from Fiquet et al., 2010), with the core and mantle composition from McDonough, 2003 (i.e. a conservative 2 wt% S in the core, 45 wt% SiO_2 and a current 20.3 ppb U in the bulk silicate Earth (BSE)), and assuming an fO_2 of IW-2, we calculate partitioning of U in the differentiating planet to be D_U = 0.026 (+0.03/-0.01) to 0.040 (+0.04/-0.02), resulting in a concentration of 1.4-2.1 ppb U in the core. It is important to note that these calculations were done for the age 4.5 Ga. Starting

393 with a current 20.3 ppb U in the BSE and integrating back through time, the U content in
394 the initial BSE equaled 53.7 ppb. This U concentration in the core would produce a
395 modest 0.6-0.9 TW of heat at the onset of core formation, and 0.10-0.15 TW at the
396 present time (Turcotte and Schubert, 2002).

397 Additionally, we confirm the strong dependence of U partitioning on S content of
398 the core discussed by previous studies (Malavergne et al., 2007; Bouhifd et al., 2013;
399 Wohlers and Wood, 2015). Raising the sulfur content of the metal to an extreme upper
400 bound of 8 wt% elevates the amount of U initially partitioned into the core at an average
401 temperature of 4200 K to 3.5 (+3/-1) ppb, corresponding to 1.4 TW of heat. We
402 emphasize, however, that high sulfur contents are not necessary to produce a significant
403 radiogenic heat source by partitioning U into the core; high *P-T* conditions alone can
404 achieve this. Figure 5 shows the amount of U partitioned into the metal as a function of
405 temperature of metal-silicate equilibration with 0 and 8 wt% S. The amount of U in the
406 core increases dramatically above 4000 K, temperatures that would be expected
407 subsequent to a large impact (Canup et al., 2015) or in a basal magma ocean (Fiquet et
408 al., 2010). The expected amount of U in the core is less if the calculations are done using
409 the liquidus of Andrault et al., 2011, because their preferred temperature profile is lower
410 than that of Fiquet et al., 2011. For example, using 3400 K, the liquidus temperature at 58
411 GPa from Andrault et al., 2011, and 2 wt% S, 0.6 ppb U is expected in the core, about
412 50% that using the higher liquidus profile.

413 ***4.3 Core formation under a range of pressures and temperatures***

414 Modeling core formation at a single representative pressure and temperature, as
415 above, is useful for comparison between partitioning studies, as well as for direct

observation of the effects of the various fitting parameters. However, the compositions of the core and mantle were set under a range of equilibrium conditions, so it is more rigorous to model core formation as a series of equilibration steps of evolving conditions. We performed a "growing-Earth" model as described in Fischer et al., 2015, but used the liquidus profile of Fiquet et al., 2010 and added S to the core, for consistency with the single *P-T* model above. Two starting compositions were used: a "reduced Earth" and an "oxidized Earth". For the reduced Earth, the initial fO_2 was set at IW-3.5, which evolved via high *P-T* reactions to IW-1.77 at the conclusion of growth. The oxidized Earth started at IW-1.5 and evolved to IW-1.24. The U parameterization from equation 5 was added to this model, along with the parameterizations found in Table 2 of Fischer et al., 2015. As expected, the results of both the reduced and oxidized models are similar to our single *P-T* case. A reduced Earth with 2-8 wt% S in the core would result in 1.9-3.0 ppb U, or 0.75-1.2 TW, in the core. The oxidized case with the same S content would result in 1.5-2.3 ppb U, or 0.59-0.91 TW.

4.3 Implications

Based on these results, U could have been an important heat-producing element in the core throughout geologic time, especially with additional contributions from K and/or Th. Given the large uncertainties in core energy and entropy models (Nimmo, 2015), it is difficult to say precisely how important this radiogenic heat source would be. The models agree that radiogenic heat contributes to the energy budget, but that it is an inefficient source of entropy available to drive the magnetic field. The high core mantle boundary (CMB) heat flow required for a thermally driven dynamo results in a very young inner core, likely less than 1 Gyr. Integrating back through time, the high heat flow would

439 derive from very high CMB temperatures, and therefore result in extensive to complete
440 mantle melting, through much of Earth's history. A radioactive heat source would allow
441 the inner core to be somewhat older. Most importantly, this heat source would make the
442 early CMB temperature lower, which would curb mantle melting. Using our maximum U
443 in the core, resulting from partitioning at 4200 K and with 8 wt% S in the core (3.5 ppb),
444 the CMB temperature would be ~50 K lower. The large dependence on equilibration
445 temperature is such that if the core were to differentiate at an average condition of 6000
446 K, the CMB temperature would be ~220 K lower. Thus, unless the core differentiated at
447 very high temperatures or there is an additional radioactive heat source such as K, there
448 was likely widespread melting in the lower mantle. An interesting result is that without a
449 radiogenic heat source in the core, early widespread lower mantle melting, along with the
450 strong incompatibility of radioactive elements in mantle minerals, would likely
451 concentrate significant amounts of radioactive elements at the CMB. A concentrated heat
452 source in this region would significantly affect the heat budget of the core and mantle by
453 lowering the heat flux out of the core, but would probably not assist in driving the
454 magnetic field (Nimmo, 2015). Additionally, metal and silicate equilibration at these very
455 high temperatures in the lowermost mantle would further promote addition of U to the
456 core; the implication of not having a radiogenic heat source in the core is that the
457 resultant high temperatures would cause a greater amount of radiogenic heat producing
458 elements in the core.

459 **5. Conclusions**

460 We have completed metal–silicate partitioning experiments on U at pressures
461 between 41 and 67 GPa and up to 5400 K, higher *P-T* conditions than have previously

been reported, and exceeding the mean conditions at which Earth's core formed. The experiments were performed at a range of fO_2 states, from IW-3.3 to IW-1.5. We found that U becomes significantly more siderophilic at high temperatures and S contents, such that it could have been an important heat source in the energy and entropy budget of the early core. Differentiation at mean conditions of 58 GPa, 4200 K and 8 wt% S in the metal (an extreme end-member composition) would result in a maximum of 1.4 TW of heat, which would reduce the CMB temperature by ~50 K 4.5 billion years ago. Increasing the temperature of differentiation to 6000 K, such as after a large impact, would increase the U content in the core substantially such that the CMB temperature would be reduced by 220 K. However, there was likely still wide spread melting in the lower mantle. In this vein, exsolution of MgO or SiO_2 as proposed by O'Rourke and Stevenson (2016) may prove to be the energy source that explains the geomagnetic field without mantle melting in the early core energy models. Additionally, we infer a reduction in the oxidation state of U to 2+ in high-pressure silicate melts, which has not been observed previously in natural samples. A lower valence could enhance the partitioning of U into the core at these extreme conditions. It would also likely affect mineral–melt partitioning of U and may result in a fractionation between U and Th at lower mantle conditions. These results lead the way for other studies of this type on lithophilic elements including K, Th, REEs and Mg, all of which would have important implications for the geochemistry and thermal history of the planet if found to be present at significant levels in the core.

References

Akahama Y. and Kawamura H. (2007) Diamond anvil Raman gauge in multimegabar pressure range. *High Press. Res.* **27**, 473–482.

Andrault D., Bolfan-Casanova N., Nigro G. Lo, Bouhifd M. A., Garbarino G. and Mezouar M. (2011) Solidus and liquidus profiles of chondritic mantle: Implication for melting of the Earth across its history. *Earth Planet. Sci. Lett.* **304**, 251–259.

Anon (1988) *Steelmaking Data Sourcebook*. Rev. Ed., Gordon and Breach Science Publishers, New York.

Badro J., Siebert J. and Nimmo F. (2016) An early geodynamo driven by exsolution of mantle components from Earth's core. *Nature*, 1–3.

Blundy J. and Wood B. (2003) Partitioning of trace elements between crystals and melts. *Earth Planet. Sci. Lett.* **210**, 383–397.

Bouhifd M. A., Andrault D., Bolfan-Casanova N., Hammouda T. and Devidal J. L. (2013) Metal-silicate partitioning of Pb and U: Effects of metal composition and oxygen fugacity. *Geochim. Cosmochim. Acta* **114**, 13–28.

Bouhifd M. A. and Jephcoat A. P. (2011) Convergence of Ni and Co metal-silicate partition coefficients in the deep magma-ocean and coupled silicon-oxygen solubility in iron melts at high pressures. *Earth Planet. Sci. Lett.* **307**, 341–348.

Boyet M. and Carlson R. W. (2005) 142Nd evidence for early (>4.53 Ga) global differentiation of the silicate Earth. *Science (80-.).* **309**, 576–581.

Campbell A. J. (2008) Measurement of temperature distributions across laser heated samples by multispectral imaging radiometry. *Rev. Sci. Instrum.* **79**, 15108.

Canup R. M., Visscher C., Salmon J. and Fegley Jr B. (2015) Lunar Volatile Depletion Due To Incomplete Accretion Within An Impact-Generated Disk. *Nat. Geosci.* **8**, 1–6.

Cartier C., Hammouda T., Boyet M. and Bouhifd M. A. (2014) Redox control of the fractionation of niobium and tantalum during planetary accretion and core formation. *Nat. Geosci.* **7**, 573–576.

Cartier C., Hammouda T., Boyet M., Mathon O., Testemale D. and Moine B. N. (2015) Evidence for Nb 2+ and Ta 3+ in silicate melts under highly reducing conditions: A XANES study. *Am. Mineral.* **100**, 2152–2158.

Corgne A., Liebske C., Wood B. J., Rubie D. C. and Frost D. J. (2005) Silicate perovskite-melt partitioning of trace elements and geochemical signature of a deep perovskitic reservoir. *Geochim. Cosmochim. Acta* **69**, 485–496.

Fiquet G., Auzende a. L., Siebert J., Corgne A., Bureau H., Ozawa H. and Garbarino G. (2010) Melting of Peridotite to 140 Gigapascals. *Science (80-.).* **329**, 1516–1518.

Fischer R. A., Nakajima Y., Campbell A. J., Frost D. J., Harries D., Langenhorst F., Miyajima N., Pollok K. and Rubie D. C. (2015) High pressure metal-silicate partitioning of Ni, Co, V, Cr, Si, and O. *Geochim. Cosmochim. Acta* **167**, 177–194.

Frost D. J., Asahara Y., Rubie D. C., Miyajima N., Dubrovinsky L. S., Holzapfel C., Ohtani E., Miyahara M. and Sakai T. (2010) Partitioning of oxygen between the Earth's mantle and core. *J. Geophys. Res. Solid Earth* **115**, 1–14.

Ganguly J. (2009) *Thermodynamics in Earth and Planetary Sciences*.,

Gomi H., Ohta K., Hirose K., Labrosse S., Caracas R., Verstraete M. J. and Hernlund J. W. (2013) The high conductivity of iron and thermal evolution of the Earth's core. *Phys. Earth Planet. Inter.* **224**, 88–103.

Kawanishi S., Yoshikawa T. and Tanaka T. (2009) Equilibrium Phase Relationship between SiC and a Liquid Phase in the Fe-Si-C System at 1523–1723 K. *Mater. Trans.* **50**, 806–813.

de Koker N., Steinle-Neumann G. and Vlcek V. (2012) Electrical resistivity and thermal conductivity of liquid Fe alloys at high P and T, and heat flux in Earth's core. *Proc. Natl. Acad. Sci. U. S. A.* **109**, 4070–4073.

Konôpková Z., McWilliams R. S., Gómez-Pérez N. and Goncharov A. F. (2016) Direct measurement of thermal conductivity in solid iron at planetary core conditions. *Nature* **534**, 99–101.

Labrosse S., Poirier J. P. and Le Mouël J. L. (2001) The age of the inner core. *Earth Planet. Sci. Lett.* **190**, 111–123.

Lay T., Hernlund J. and Buffett B. (2008) Core–mantle boundary heat flow. *Nat. Geosci.* **1**, 25–32.

Li J. and Agee C. B. (2001) The effect of pressure, temperature, oxygen fugacity and composition on partitioning of nickel and cobalt between liquid Fe-Ni-S alloy and liquid silicate: Implications for the Earth's core formation. *Geochim. Cosmochim. Acta* **65**, 1821–1832.

Li Y., Dasgupta R. and Tsuno K. (2015) The effects of sulfur, silicon, water, and oxygen fugacity on carbon solubility and partitioning in Fe-rich alloy and silicate melt systems at 3 GPa and 1600 ??C: Implications for core-mantle differentiation and degassing of magma oceans and reduced plane. *Earth Planet. Sci. Lett.* **415**, 54–66.

MacDonald M. R., Fieser M. E., Bates J. E., Ziller J. W., Furche F. and Evans W. J. (2013) Identification of the +2 Oxidation State for Uranium in a Crystalline Molecular Complex, [K(2.2.2-Cryptand)][(C 5 H 4 SiMe 3) 3 U]. *J. Am. Chem. Soc.* **135**, 13310–13313.

Malavergne V., Tarrida M., Combes R., Bureau H., Jones J. and Schwandt C. (2007) New high-pressure and high-temperature metal/silicate partitioning of U and Pb: Implications for the cores of the Earth and Mars. *Geochim. Cosmochim. Acta* **71**, 2637–2655.

McDonough W. F. (2003) Compositional Model for the Earth's Core. In *Treatise On Geochemistry* (eds. H. D. Holland and K. K. Turekian). Elsevier Ltd. pp. 547–568.

McDonough W. F. and Sun S. s. (1995) The composition of the Earth. *Chem. Geol.* **120**, 223–253.

Miettinen J. (1998) Reassessed thermodynamic solution phase data for ternary Fe-Si-C system. *Calphad* **22**, 231–256.

Nimmo F. (2015) *Energetics of the Core*., Elsevier B.V.

O'Neill H. S. C. and Eggins S. M. (2002) The effect of melt composition on trace element partitioning: An experimental investigation of the activity coefficients of FeO, NiO, CoO, MoO2 and MoO3 in silicate melts. *Chem. Geol.* **186**, 151–181.

O'Rourke J. G. and Stevenson D. J. (2016) Powering Earth's dynamo with magnesium precipitation from the core. *Nature* **529**, 387–389.

Ohta K., Kuwayama Y., Hirose K., Shimizu K. and Ohishi Y. (2016) Experimental determination of the electrical resistivity of iron at Earth's core conditions. *Nature* **534**, 95–98.

Pozzo M., Davies C., Gubbins D. and Alfè D. (2012) Thermal and electrical conductivity of iron at Earth's core conditions. *Nature* **485**, 355–358.

Pozzo M., Davies C., Gubbins D. and Alfè D. (2014) Thermal and electrical conductivity of solid iron and iron–silicon mixtures at Earth's core conditions. *Earth Planet. Sci. Lett.* **393**, 159–164.

Righter K. (2003) Metal–silicate partitioning of siderophile elements and core formation in the early Earth. *Annu. Rev. Earth Planet. Sci.* **31**, 135–174.

Righter K., Danielson L. R., Pando K. M., Shofner G. A., Sutton S. R., Newville M. and Lee C.-T. (2016) Valence and metal/silicate partitioning of Mo: Implications for conditions of Earth accretion and core formation. *Earth Planet. Sci. Lett.* **437**, 89–100.

Sanloup C. and Fei Y. (2004) Closure of the Fe-S-Si liquid miscibility gap at high pressure. *Phys. Earth Planet. Inter.* **147**, 57–65.

Seagle C. T., Cottrell E., Fei Y., Hummer D. R. and Prakapenka V. B. (2013) Electrical and thermal transport properties of iron and iron-silicon alloy at high pressure. *Geophys. Res. Lett.* **40**, 5377–5381.

Siebert J., Badro J., Antonangeli D. and Ryerson F. J. (2012) Metal-silicate partitioning of Ni and Co in a deep magma ocean. *Earth Planet. Sci. Lett.* **321**–**322**, 189–197.

Turcotte D. L. and Schubert G. (2002) *Geodynamics*. 2nd ed., Cambridge University Press.

Verhoogen J. (1980) *Energentics of the Earth*., National Academy Press, Washington, D.C.

Wade J. and Wood B. J. (2005) Core formation and the oxidation state of the Earth. *Earth Planet. Sci. Lett.* **236**, 78–95.

Wade J. and Wood B. J. (2012) Metal-silicate partitioning experiments in the diamond anvil cell: A comment on potential analytical errors. *Phys. Earth Planet. Inter.* **192**–**193**, 54–58.

Wohlers A. and Wood B. J. (2015) A Mercury-like component of early Earth yields uranium in the core and high mantle (142)Nd. *Nature* **520**, 337–40.

Acknowledgments: This work was funded by a NSF Graduate Research Fellowship Grant #DGE-1144082, NSF Grant #EAR-1427123, and an RTOP through the NASA Cosmochemistry Program. The FIB and TEM work were completed in the Electron Beam Analysis Labs within the Astromaterials Research and Exploration Science office at Johnson Space Center. The authors thank four anonymous reviewers and the associate editor, Munir Humayun, for helpful comments. B.A.C. thanks R. Fischer and N. Dauphas for helpful discussions.

Table Captions

Table 1: Starting compositions in weight % for the metal and silicate portions of each sample. Samples B22 and B23 were structured in such a way that the starting composition could not be estimated in this way – see text.

Table 2: Experimental conditions for the DAC samples. Oxygen fugacity (fO_2) was calculated using the mole fractions of Fe and FeO and assuming ideality. Partition coefficents (D_U) and exchange coefficents (K_D) were calculated using mole fractions.

Table 3: Metal phase compositions in both mole percent and weight percent for the samples in this study. Standard errors are given on the least significant digit. “n” is the number of measurements. Asterisks indicate oxygen contents that were calculated rather

than measured – see text. If an element was below the detection limit, it is denoted as "nd". Elements with 0 percent were not present in the sample material. Ca and Th are not included in this table because they were not detectable by EDX in any of the metallic phases of the samples studied.

Table 4: Silicate melt compositions in both mole percent and weight percent. Errors are either the standard errors of the average or the error from the point spread analysis. Elements with 0 percent were not present in the sample material. †Either the number of measurements or "PS" indicating a fit using the point spread function.

Table 5: Metal–silicate partitioning parameters fit to Eqs. 5 and 6 for U. The root-mean-square (RMS) misfit to the data is 0.31 log units in both cases. The data (n=20) are listed in Table A.1.

Figure Captions

Fig. 1: **(Top left)** Transmission electron image of sample B42, recovered from 57 GPa and 3800 K. The dark region contains metallic and silicate melts; the bright region is amorphous $MgSiO_3$ that was bridgmanite under high P conditions. **(Bottom left)** Composite X-ray map of Fe, U and Si. **(Right)** X-ray maps for individual elements.

Fig. 2: **a)** Back-scattered electron image of sample B50. Sample recovered from 56 GPa and 4700 K. Red arrow indicates location of EDX profile. **b)** EDX profiles of U, Ca and Fe across sample B50. Measurements were made in 0.25 μm steps.

Fig. 3: Plot of partition coefficients as a function of $fO_2(\Delta IW)$. Orange symbols are sulfur-containing samples. All of the data have been corrected to 3000 K with 2 wt% S in the metal and 45 wt% SiO_2 in the silicate melt. Lines of slope -1 (indicating U^{4+}) and -0.5 (indicating U^{2+}) are included for reference.

Fig. 4: Temperature dependence of metal–silicate partitioning of U. Orange symbols are sulfur-containing samples. Solid lines represent the expected exchange coefficients at constant sulfur content in the metal in weight percent. Inset: Residuals to the fit.

Fig. 5. U content and the resulting heat production at the onset of core formation as a function of metal-silicate equilibration temperature. Black line: 0 wt% S in the metal; orange line: 8 wt% S. Error envelopes are derived from the root-mean-squared error on the fit.

Appendix Table Captions

Table A.1. Data from the literature and this study used in fitting thermodynamic parameters of partitioning.

669 Table A.2. Metallic compositions of the samples in this study in mole percent element.
670 The number of point measurements included in average and error calculations is noted.
671 Asterisks indicate calculated oxygen contents – see text.
672
673 Table A.3. Silicate compositions of the samples in this study in mole percent oxide. It is
674 noted if composition was determined by point spread analysis, and if not, the number of
675 point measurements included in average and error calculations is noted. Dashes indicate
676 materials that were not included in the samples.
677
678 **Appendix Figure Captions**
679
680 Figure A.1. Illustration of signal deconvolution of the Fe signal in each phase using
681 point-spread analysis. For comparison of spatial resolution, top panel was measured on
682 the TEM at Johnson Space Center; bottom panel are measurements from the Tescan SEM
683 at the University of Chicago. Filled circles are the measurements, green x's are the fitted
684 compositions of Fe in each phase, dashed lines are the fitted boundaries between phases.
685
686
687

688 **Table 1**

Sample #	Metal	Silicate				
		MgO	**Al_2O_3**	**$CaSiO_3$**	**SiO_2**	**UO_2**
B42	FeSi	36.56	8.40	0	43.44	11.60
B49	Fe–12S–22Si	35.35	8.13	6.85	38.46	11.22
B50	FeSi	35.35	8.13	6.85	38.46	11.22
B56	FeSi	35.35	8.13	6.85	38.46	11.22
B66	Fe–4S–15Si	35.35	8.13	6.85	38.46	11.22

689

690 **Table 2**

Sample	P (GPa)	+/-	T (K)	+/-	fO_2 (ΔIW)	+	-	D_U	+/-	K_D	+/-
B22	67	6	4700	400	-2.1	0.01	-0.01	0.0328	0.0003	0.00294	0.00005
B23	61	6	5000	300	-2.62	0.03	-0.04	0.0441	0.0003	0.00216	0.00009
B42	57	6	3800	200	-2.15	0.05	-0.05	0.039	0.001	0.0032	0.0002
B49	55	5	5400	300	-1.53	0.03	-0.03	0.662	0.004	0.114	0.004
B50	57	6	4800	300	-3.3	0.2	-0.2	0.23	0.01	0.005	0.001
B56	41	5	4000	200	-3.19	0.02	-0.02	0.042	0.002	0.00107	0.00005
B66	54	5	4400	300	-2.12	0.06	-0.07	0.23	0.004	0.02	0.002

691

692 **Table 3**

Sample		Fe	Si	O	S	Al	Mg	U	n
B22	mol%	57.27(5)	33.04(4)	8.34(5)	0	nd	0	1.36(1)	261
	wt%	69.78(6)	20.25(2)	2.9(2)	0	nd	0	7.06(5)	
B23	mol%	47.16(5)	42.51(4)	8.65(5)	0	0.1(1)	0	1.54(1)	91
	wt%	60.75(6)	27.54(3)	3.19(2)	0	0.06(6)	0	8.45(5)	
B42	mol%	48.7(1)	44.6(1)	5.26*	0	0.23(2)	0.76(7)	0.45(1)	13
	wt%	64.9(1)	29.91(7)	2.01*	0	0.15(1)	0.44(4)	2.56(6)	
B49	mol%	33.4(4)	18.31(2)	21.28(6)	19.84(3)	0.949(8)	2.92(1)	3.299(8)	126
	wt%	44.01(5)	12.14(1)	8.03(2)	15.01(2)	0.605(5)	1.675(6)	18.53(4)	
B50	mol%	57.7(1)	37.29(8)	2.54*	0	0.75(2)	1.24(8)	0.439(5)	29
	wt%	72.2(1)	23.46(5)	0.91*	0	0.45(1)	0.68(4)	2.34(3)	
B56	mol%	50.4(6)	47.22(6)	1.93*	0	0.2(1)	0.1(1)	0.122(5)	151
	wt%	66.89(8)	31.50(4)	0.73*	0	0.13(6)	0.06(6)	0.69(3)	
B66	mol%	66.36(8)	8.30(2)	19.51(7)	3.89(2)	0.30(1)	1.06(3)	0.580(8)	40
	wt%	81.36(8)	5.13(1)	6.86(2)	2.74(1)	0.18(1)	0.57(2)	3.04(4)	

693
694

695 **Table 4**

Sample		MgO	$AlO_{1.5}$	SO_3	SiO_2	CaO	FeO	ThO_2	UO	n[†]
B22	mol%	0	8.89(6)	0	39.46(9)	0	5.13(8)	5.16(3)	41.37(7)	251
	wt%	0	3.01(2)	0	15.74(4)	0	2.45(4)	9.04(5)	69.8(1)	
B23	mol%	0	7.63(8)	0	45.8(1)	0	2.31(9)	9.44(5)	34.82(9)	57
	wt%	0	2.66(3)	0	18.79(4)	0	1.13(4)	17.02(9)	60.4(2)	
B42	mol%	28.4(2)	13.7(1)	0	42.0(2)	0	4.1(2)	0	11.7(1)	PS
	wt%	15.0(1)	9.15(7)	0	33.1(2)	0	3.9(2)	0	38.9(3)	
B49	mol%	40.5(1)	10.5(1)	4.9(1)	31.6(1)	1.85(2)	5.8(2)	0	4.98(3)	PS
	wt%	26.14(6)	8.57(8)	6.3(1)	30.4(1)	1.66(2)	6.7(2)	0	20.3(1)	
B50	mol%	48.72(9)	17.9(4)	0	27(2)	3.15(5)	1.2(3)	0	1.94(9)	PS
	wt%	37.38(7)	17.4(4)	0	31(2)	3.36(5)	1.6(4)	0	9.4(4)	
B56	mol%	33.59(3)	9.03(3)	0	49.47(4)	3.73(2)	1.28(3)	0	2.90(1)	79
	wt%	23.25(2)	7.90(3)	0	51.03(4)	3.59(2)	1.58(4)	0	12.65(4)	
B66	mol%	43.6(2)	8.98(7)	2.13(3)	35.7(1)	1.32(2)	5.8(4)	0	2.52(2)	PS
	wt%	31.0(1)	8.09(6)	3.01(4)	37.9(1)	1.31(2)	7.4(5)	0	11.31(9)	

696

Table 5

	Equation 5		Equation 6	
Parameter	**Value**	**Error (±)**	**Value**	**Error (±)**
a	**0.10**	**0.3**	**0.10**	**0.3**
b	**-11,000**	**1000**	**-11,000**	**1000**
c	**-4700**	**900**	**-4700**	**800**
d	**13,000**	**3000**	**13,000**	**3000**
e	**-0.49**	**0.07**	**–**	**–**

699 **Figure 1**

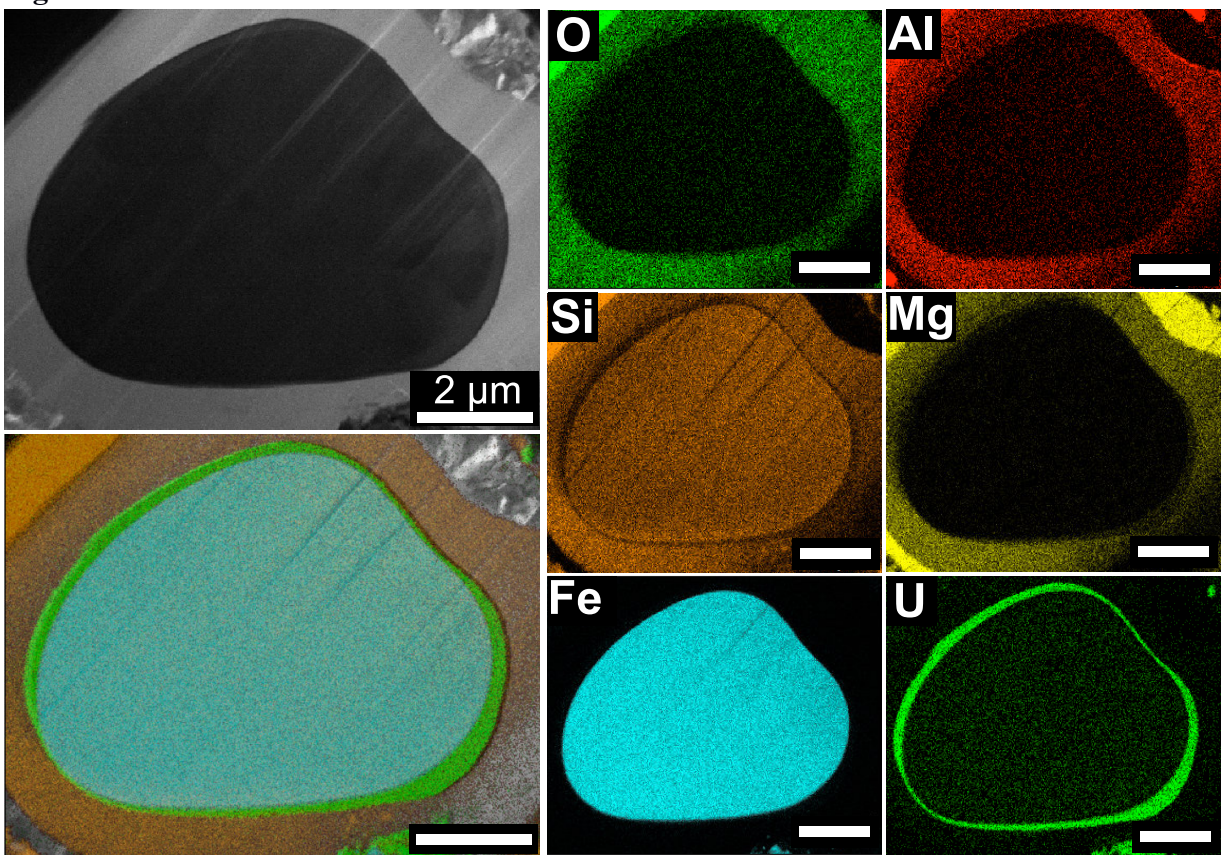

700

701 **Figure 2**

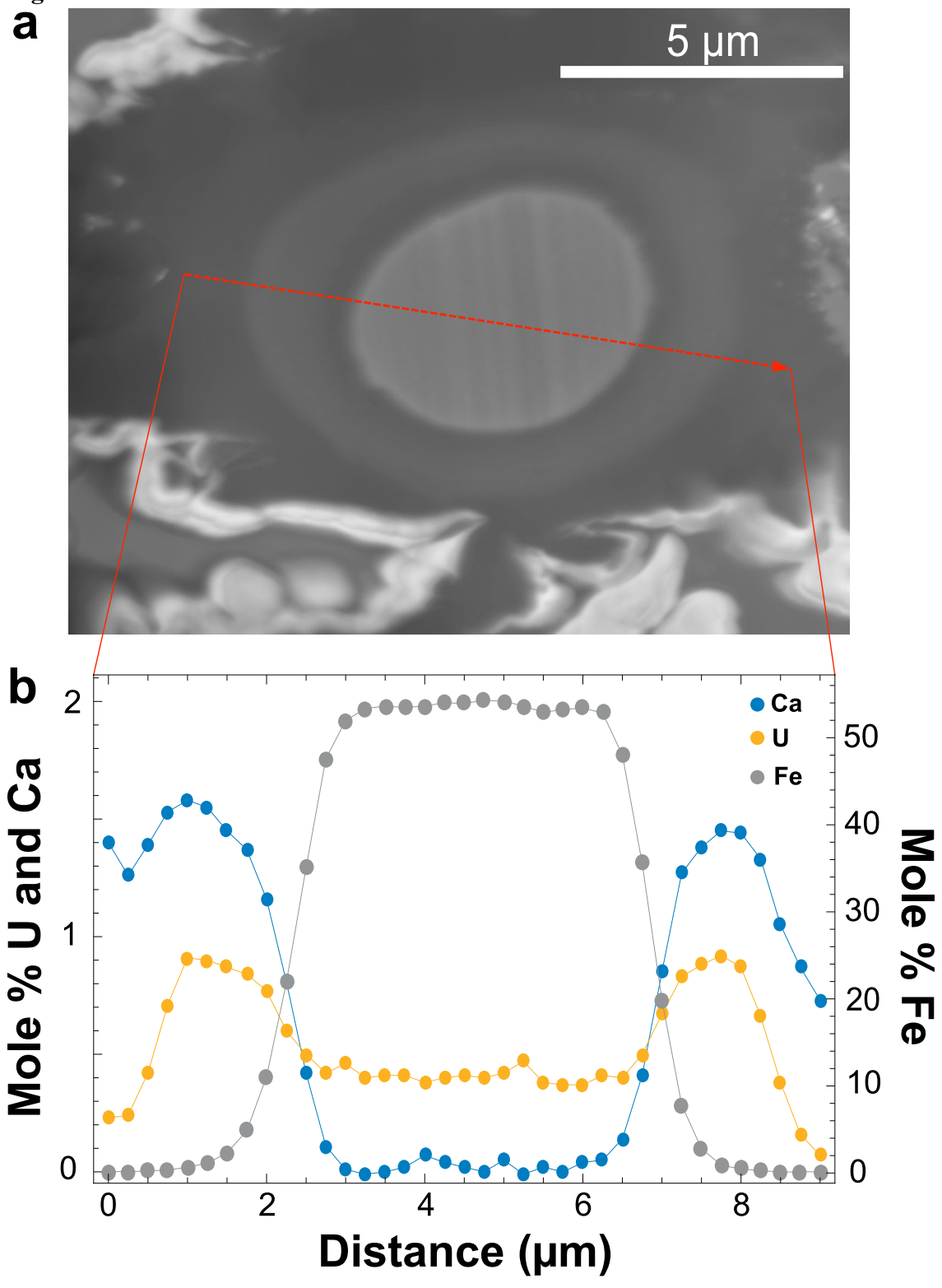

702
703

704 **Figure 3**

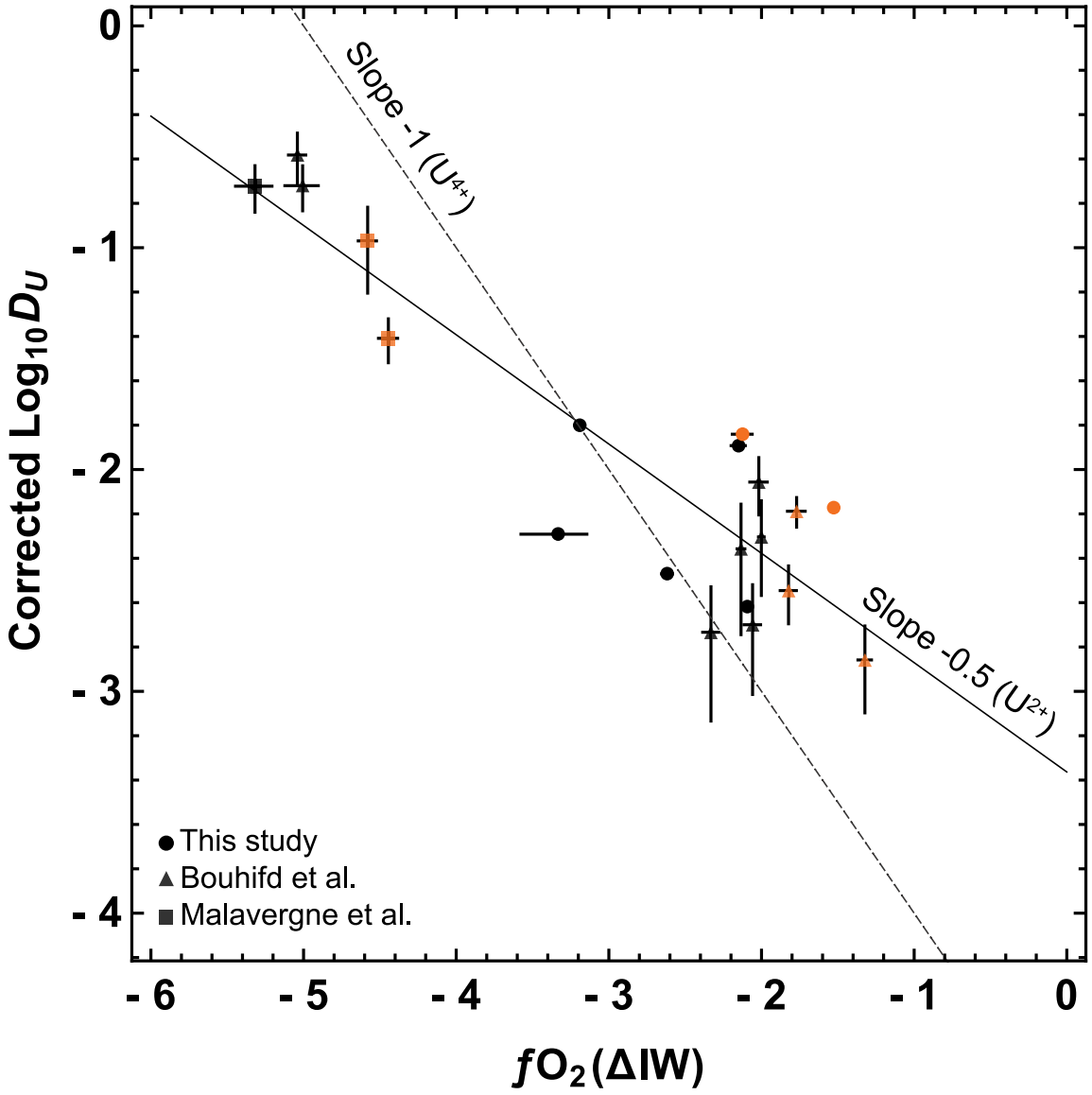

705

706 **Figure 4**

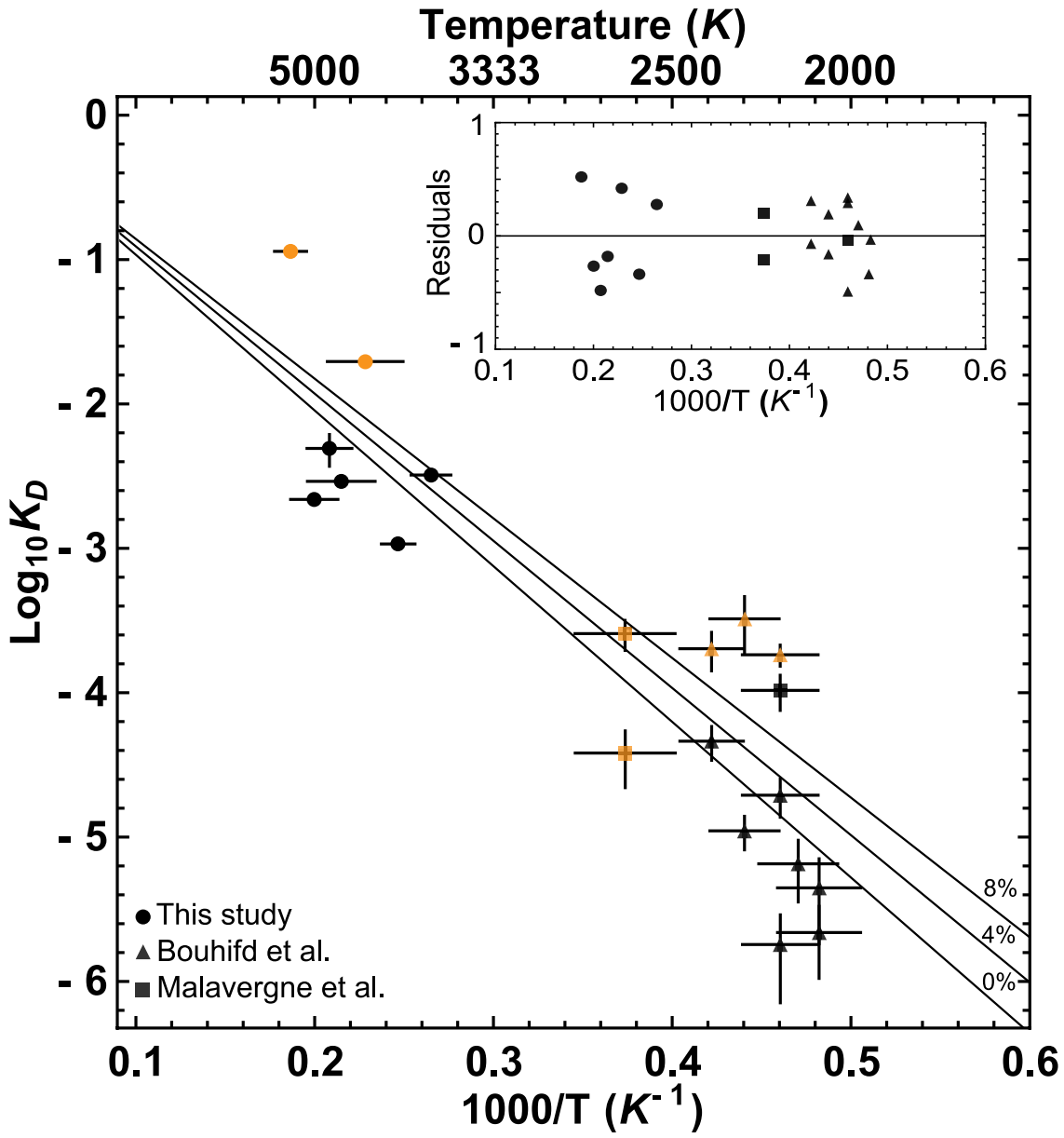

707
708
709

710 **Figure 5**

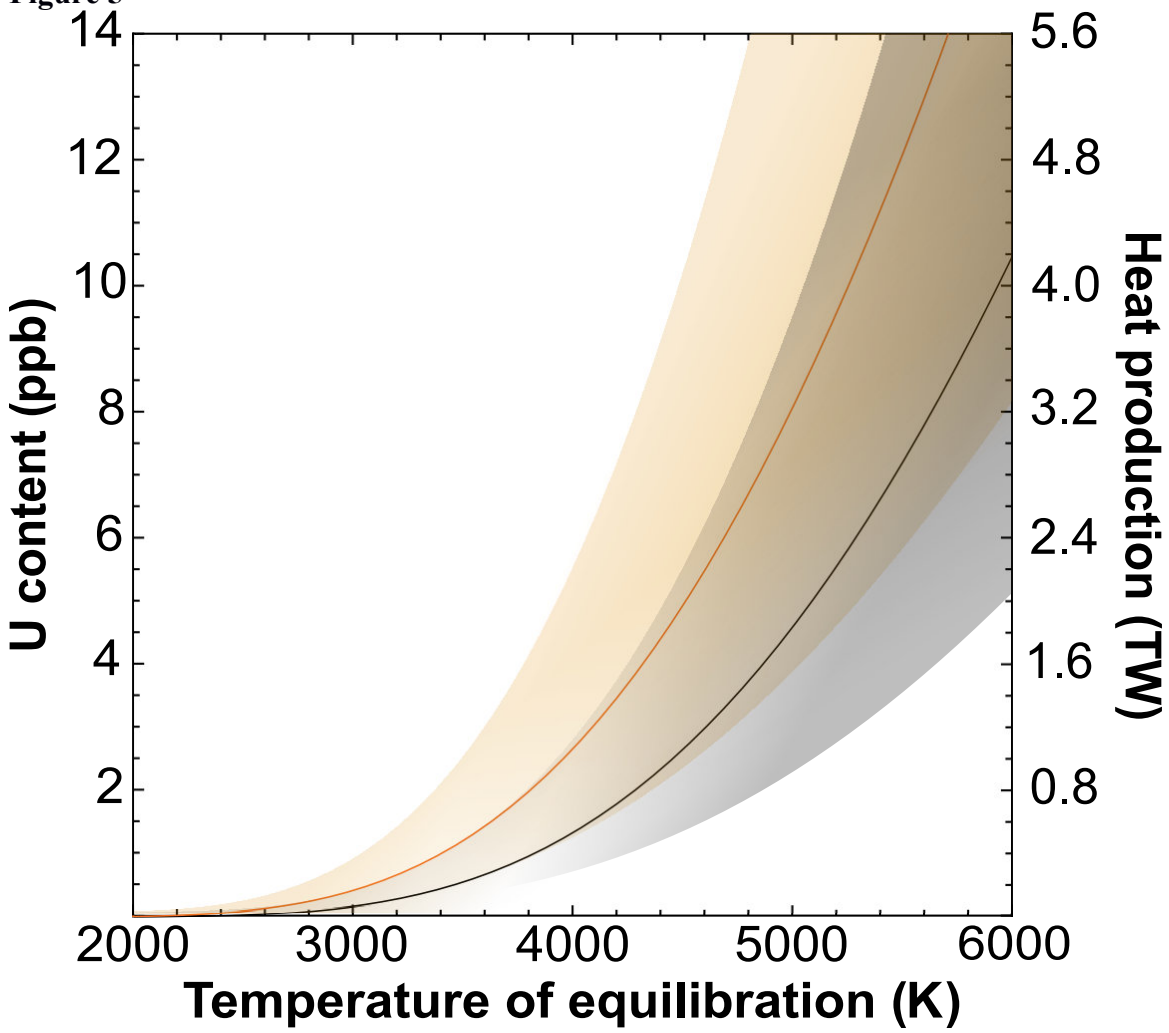

711
712

713 **Fig. A.1**

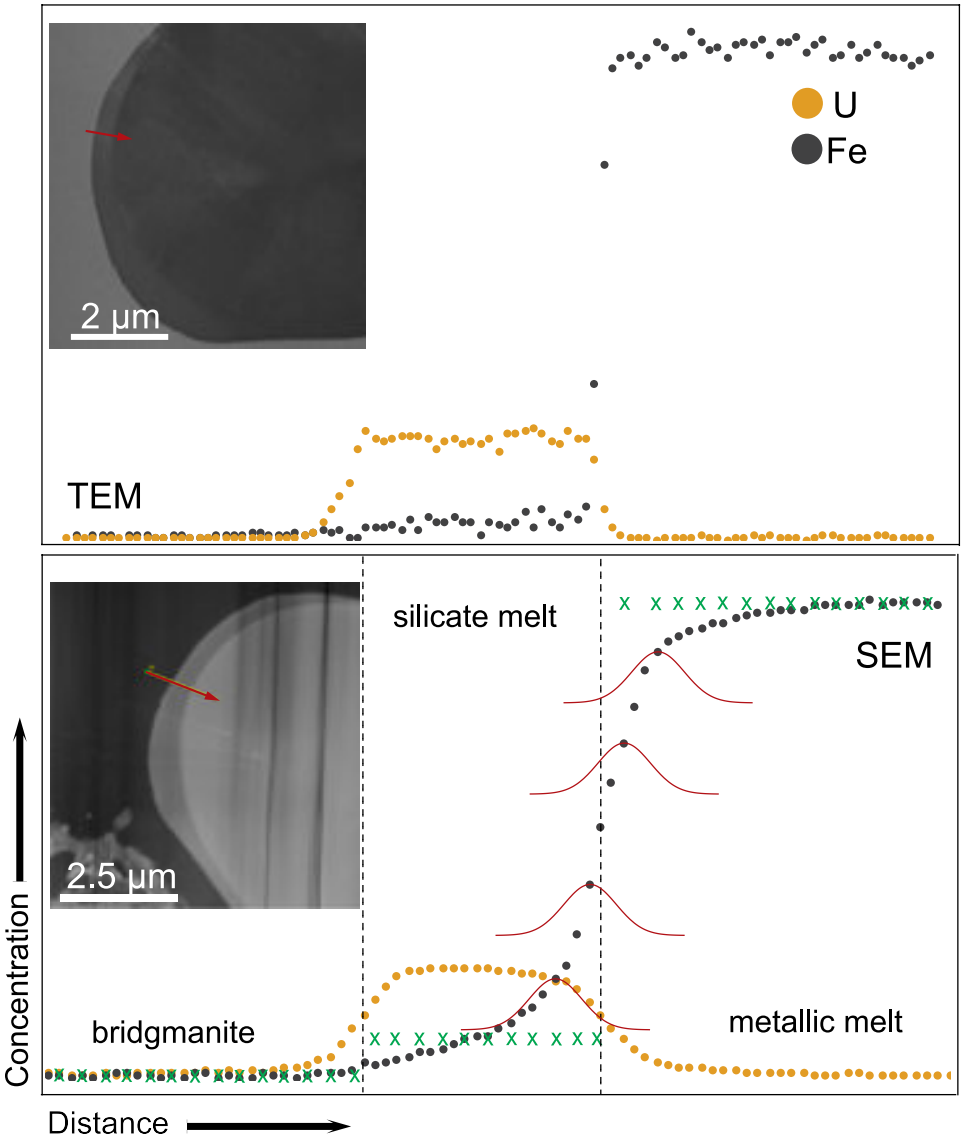

714

715

716